The Combined Effect of Spin-Transfer Torque and Voltage-Controlled Strain Gradient on Magnetic Domain-Wall Dynamics: Toward Tunable Spintronic Neuron

Guo-Liang Yu(郁国良)[1,2*], Xin-Yan He(何鑫岩)[1], Sheng-Bin Shi(施胜宾)[3], Yang Qiu(邱阳)[1,2], Ming-Min Zhu(朱明敏)[1,2], Jia-Wei Wang(王嘉维)[1,2], Yan Li(李燕)[1,2], Yuan-Xun Li(李元勋)[4], Jie Wang(王杰)[3*], and Hao-Miao Zhou(周浩淼)[1,2*]

[1]*College of Information Engineering, China Jiliang University, Hangzhou 310018, China*
[2]*The Key Laboratory of Electromagnetic Wave Information Technology and Metrology of Zhejiang Province, Hangzhou 310018, China*
[3]*Department of Engineering Mechanics, Zhejiang University, Hangzhou 310027, China*
[4]*School of Electronic Science and Engineering, University of Electronic Science and Technology of China, Chengdu 611731, China*

(Received 21 January 2024; accepted manuscript online 17 April 2024)

Magnetic domain wall (DW), as one of the promising information carriers in spintronic devices, have been widely investigated owing to its nonlinear dynamics and tunable properties. Here, we theoretically and numerically demonstrate the DW dynamics driven by the synergistic interaction between current-induced spin-transfer torque (STT) and voltage-controlled strain gradient (VCSG) in multiferroic heterostructures. Through electromechanical and micromagnetic simulations, we show that a desirable strain gradient can be created and it further modulates the equilibrium position and velocity of the current-driven DW motion. Meanwhile, an analytical Thiele's model is developed to describe the steady motion of DW and the analytical results are quite consistent with the simulation data. Finally, we find that this combination effect can be leveraged to design DW-based biological neurons where the synergistic interaction between STT and VCSG-driven DW motion as integrating and leaking motivates mimicking leaky-integrate-and-fire (LIF) and self-reset function. Importantly, the firing response of the LIF neuron can be efficiently modulated, facilitating the exploration of tunable activation function generators, which can further help improve the computational capability of the neuromorphic system.

DOI: 10.1088/0256-307X/41/5/057502

Magnetic domain walls (DWs) have attracted great attention with unique nonlinear properties and potential application in racetrack memories,[1,2] logics,[3–5] nano-oscillators,[6–8] and artificial-intelligence neuromorphic devices.[9–14] The basic operation of the above applications is governed by the controlled motion of DWs. Consequently, many external stimuli have been studied that serve as driving forces, such as currents,[15,16] magnetic fields,[17–19] electric fields,[20] spin waves,[21] and other physical fields.[22–24] Among these, the current-driven DW motion has shown promising features for emulating various biological synaptic and neural characteristics.[25–27]

Spintronic devices based on magnetic solitons (e.g., DW, skyrmion) with the advantages of high speed and low power consumption have shown great potential for developing artificial neuromorphic computing systems.[28–30] Compared to skyrmion, which is difficult to generate, manipulate, and detect, DW-based neuromorphic devices are easier to realize experimentally.[27,31] Promoted as one of the most applicable models of artificial neurons, the DW-based leaky-integrate-and-fire (LIF) function has recently attracted widespread attention in artificial neural devices and spiking neural networks (SNNs).[27,32–34] In such a DW-based artificial neuron, the temporary position of the DW can be analogously characterized as the membrane potential of a biological neuron. Once the membrane potential reaches a defined threshold, the neuron fires an output spike and then resets by applying another opposite sign current. However, this current-driven reset approach is not energy-efficient. To overcome this limitation, several methods have been proposed, such as introducing shape anisotropy to induce spontaneous DW motion,[35] engineering perpendicular anisotropy gradients to perform intrinsic leaky,[36,37] creating lateral inhibition to make the neuron perform characters intrinsically,[38] and introducing a build-in field of the reference layer to mimic the self-reset characteristics of biological neurons.[27,31] However, these spiking neurons generally exhibit fixed characteristics and it is difficult to adjust the function to adapt to the system variation. However, biological neurons always feature a configurable activation function to perform calculation tasks, tuned by modulatory stimuli.[39] In this regard, recent experimental and theoretical works have shown that the inclusion of adjustable LIF neurons in SNN can improve their computational capabilities.[40,41] To allow broader applicability of DW-based neuron devices, an

*Corresponding authors. Email: glyu@cjlu.edu.cn; jw@zju.edu.cn; zhouhm@cjlu.edu.cn
© 2024 Chinese Physical Society and IOP Publishing Ltd

effective procedure for modulating DW independent of the current is urgently needed.

Recent studies have found that non-uniform stress can drive DW motion in a strain-mediated multiferroic heterostructure.[42,43] Also, our previous work shows that DW propagation in a multiferroic heterostructure can be dynamically modulated by voltage-controlled strain gradient (VCSG).[44] On the basis of the above perspective, we combine electromechanical and micromagnetic simulations to demonstrate the synergistic interaction between current-induced spin-transfer torque (STT) and VCSG on the DW motion to mimic the LIF and self-reset function of artificial neurons. Dynamics characteristics and the response of DW, including the effects of Gilbert damping, VCSG strength, and current density on the DW velocity and equilibrium position are presented. Analytical Thiele's model of the dynamic behavior of DW under the combined effect of STT and VCSG is established. Results show that the correlation between the steady velocity of DW, current density, and VCSG strength can be well captured by the analytical model. Especially, by choosing an appropriate current and VCSG strength, DW-based artificial neurons with slope-tunable activation functions and tunable firing frequency characters are obtained.

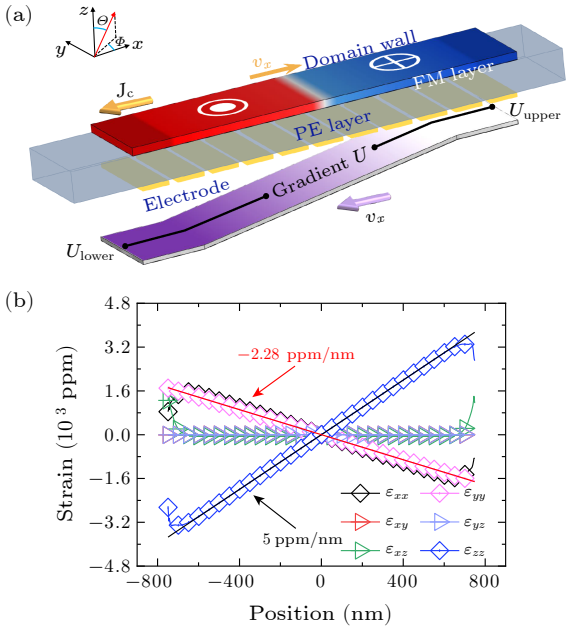

Fig. 1. (a) Schematic diagram of the proposed device. The origin of the coordinates is located in the center of the FM layer. (b) Profile of the strain tensor components in the FM layer. The symbol represents the simulation results and the solid line represents a linear fitting.

Model and Method. Figure 1(a) shows a schematic diagram of the proposed device structure, which consists of a perpendicular anisotropy (PMA) ferromagnetic (FM) heterostructure deposited on a piezoelectric (PE) substrate layer with a series of electrodes at the bottom of the PE substrate. By shifting the DW position via current-induced STT, we can in principle continuously vary the DW position by the MTJ conductance[45] or anomalous Hall resistance[46] as the biological signals. In the following discussion, for simplicity, we choose the intermediate position x of the DW as the biological signal. In addition to the current, variation of strain is achieved by controlling the voltage applied to the series electrodes, and then this strain is transferred to the FM layer which can be used in modulating the DW dynamics similar to the current. Here, the CoFeB, PZT-5H, and Au are chosen as the FM, PE, and electrode materials, respectively. Considering that we want to implement the self-rest, leaking, and tuning behavior of the devices, the current and VCSG need to produce DW motion in the opposite direction.

The strain distribution is calculated by COMSOL Multiphysics, where the CoFeB sample is $1500 \times 150 \times 1\,\text{nm}^3$, and the PE substrate has the same in-plane dimensions but with a thickness of 100 nm. A total number of 25 electrodes with 40 nm width and 60 nm spacing are placed in series at the bottom of the PE layer, see the inset of Fig. S1(a) in Section S1 of the Supplementary Material. The parameters of the PZT-5H and Au are directly derived from the material library. Meanwhile, elastic stiffness coefficients and Poison ratio of CoFeB are $c_{11} = 218.1\,\text{GPa}$, $c_{12} = 93.46\,\text{GPa}$, $c_{44} = (c_{11} - c_{12})/2 = 62.32\,\text{GPa}$, and $v = 0.3$.[47]

Figure 1(b) shows the strain profiles along the length direction at the center of the FM. Here, a linear varying voltage value described by the function $U = ax$ with $a = 1.29\,\text{V}/\mu\text{m}$ is applied, where the x follows the central-position values of series electrodes. As can be observed, the dominant component varies linearly in the central region of FM except at two length ends. Note that the in-plane strain gradient components, i.e., $\partial\varepsilon_{xx}/\partial x$ and $\partial\varepsilon_{yy}/\partial x$, are approximately equal to each other, while the out-of-plane component $\partial\varepsilon_{zz}/\partial x$ is about twice the time of in-plane components and with opposite signs. The other three non-main components are so small that their effects on the DW dynamics can be further neglected. For simplicity, we are using $\partial\varepsilon_{zz}/\partial x$ for the presentation in the following discussions. More details about the VCSG of this proposed structure can be found in Section S1 of the Supplementary Material.

The dynamics of magnetization are governed by the Landau–Lifshitz–Gilbert (LLG) equation with STT and magnetoelastic coupling

$$\frac{\partial \boldsymbol{m}}{\partial t} = -\gamma_0 \boldsymbol{m} \times (\boldsymbol{H}_{\text{eff}} + \boldsymbol{H}_{\text{me}}) + \alpha \boldsymbol{m} \times \frac{\partial \boldsymbol{m}}{\partial t} + \tau_{zl}, \quad (1)$$

where $\boldsymbol{m} = \boldsymbol{M}/M_{\text{s}}$ is the normalized magnetization, $\boldsymbol{M}$ is the magnetization, M_{s} is the saturation magnetization, $\gamma_0 = \mu_0\gamma$ with $\gamma = g|e|/2m_{\text{e}}$ is the gyromagnetic ratio, g is the Landé factor, e is the electron charge, m_{e} is the electron mass, and α is the Gilbert damping coefficient. $\boldsymbol{H}_{\text{eff}}$ is the effective field, includes the exchange, PMA, iDMI, demagnetization, and the Zeeman interactions, and the magnetoelastic effective field $\boldsymbol{H}_{\text{me}}$ can be expressed as[48]

$$\boldsymbol{H}_{\text{me}} = -\frac{2}{\mu_0 M_{\text{s}}} \begin{pmatrix} B_1\varepsilon_{xx}m_x + B_2(\varepsilon_{xy}m_y + \varepsilon_{xz}m_z) \\ B_1\varepsilon_{yy}m_y + B_2(\varepsilon_{xy}m_x + \varepsilon_{yz}m_z) \\ B_1\varepsilon_{zz}m_z + B_2(\varepsilon_{xz}m_x + \varepsilon_{yz}m_y) \end{pmatrix}, \quad (2)$$

where B_1 and B_2 are magnetoelastic coupling constants.

The τ_{zl} describes the Zhang–Li type STT, which is given by

$$\tau_{zl} = -\gamma_0 \boldsymbol{m} \times \boldsymbol{H}_{\rm ad}^{\rm STT} - \gamma_0 \boldsymbol{m} \times \boldsymbol{H}_{\rm nad}^{\rm STT}, \tag{3}$$

where $\boldsymbol{H}_{\rm ad}^{\rm STT} = \boldsymbol{m} \times (u\boldsymbol{J} \cdot \nabla)\boldsymbol{m}$ is the adiabatic effective field, $u = P\hbar/2|e|\mu_0 M_{\rm s}(1+\beta^2)$, $\boldsymbol{J}$ is the current, P is the spin polarization, and $\hbar$ is the reduced Planck constant. The $\boldsymbol{H}_{\rm nad}^{\rm STT} = (\beta u \boldsymbol{J} \cdot \nabla)m$ is the non-adiabatic magnetic field, and β is the non-adiabatic coefficient. The Mumax^3 package is performed for the micromagnetic simulations and the parameters of CoFeB are chosen as follows: $M_{\rm s} = 1100\,{\rm kA/m}$, $A_{\rm ex} = 19\,{\rm pJ/m}$, $P = 0.3$, $\beta = 0.02$, iDMI $= 1.0\,{\rm mJ/m^2}$, and $K_{\rm u} = 1\,{\rm MJ/m^3}$.[49–51] B_1 and B_2 can be expressed by the magnetostriction λ_{100} and λ_{111}, as well as the c_{ij}, i.e., $B_1 = -3\lambda_{100}(c_{11}-c_{12})/2$ and $B_2 = -3\lambda_{111}c_{44}$, and $\lambda_{100} = \lambda_{111} = \lambda_{\rm s} = 37\,{\rm ppm}$.[52] Moreover, to be able to make the micromagnetic simulation of the magnetoelastic coupling effect and the piezoelectric strain cause corresponding, we have imported the spatial distribution of the strain into the micromagnetic simulation.

Furthermore, we also derive a 1DM Thiele's equation for steady-state DW motion (see Sections S2 and S3 of the Supplementary Material for details)

$$-D_{xx}(\alpha v_x + \beta u_0 J_x) + F_x^{\rm ME} = 0, \tag{4}$$

where

$$\begin{aligned} &D_{xx} = \frac{\mu_0 M_{\rm s}}{\gamma_0} t_{\rm f} \iint dxdy \left(\frac{\partial \boldsymbol{m}}{\partial x} \cdot \frac{\partial \boldsymbol{m}}{\partial x}\right), \\ &u_0 = \gamma_0 u, \quad F_x^{\rm D} = -\alpha D_{xx} v_x, \quad F_x^{\rm STT} = -\beta D_{xx} u_0 J_x, \\ &F_x^{\rm ME} = t_{\rm f} \iint dxdy \Big(\sum_{i=x,y,z} 2B_1 \varepsilon_{ii} m_i \frac{\partial m_{x_i}}{\partial x} \\ &\quad + \sum_{\substack{i\neq j \\ x,y,z}} 2B_2 \varepsilon_{ij} m_i \frac{\partial m_{x_j}}{\partial x} \Big), \end{aligned}$$

with $F_x^{\rm D}$, $F_x^{\rm STT}$, and $F_x^{\rm ME}$ representing the dissipative force, the STT force, and the magnetoelastic force, respectively. Thus, the steady velocity can be derived from Eq. (4) expressed as

$$v_x = \frac{1}{\alpha}\left(\frac{F_x^{\rm ME}}{D_{xx}} - \beta u_0 J_x\right), \tag{5}$$

To elucidate the micromagnetic simulation results, the expressions of D_{xx} and $F_x^{\rm ME}$ need to be explicitly, then we choose the following ansatz for the Néel type DW:[23]

$$\begin{aligned} &\Theta(x) = 2\tan^{-1}\exp\left[Q_{\rm w}\frac{x-q}{\Delta}\right] \\ &\Phi(x) = \phi, \end{aligned} \tag{6}$$

with $\boldsymbol{m} = (\sin\Theta\cos\Phi, \sin\Theta\sin\Phi, \cos\Theta)$. Here Θ and Φ are the polar and azimuthal angles of the local magnetization as shown in Fig. 1(a); q is the DW position, $\Delta = \sqrt{A/K_0}$ is the DW width parameter with $K_0 = K_{\rm u} - \mu_0 M_{\rm s}^2/2$. The parameter $Q_{\rm w}$ is selected as $+1$ if the domain wall configuration is up-down ($\uparrow\downarrow$, present work) and -1 if down-up ($\downarrow\uparrow$) from the left to right along the x-axis direction. Thus, the explicitly expressions of D_{xx} and $F_x^{\rm ME}$ read

$$D_{xx} = 2\frac{\mu_0 M_{\rm s}}{\gamma_0 \Delta} w_{\rm f} t_{\rm f} \tag{7}$$

$$F_x^{\rm ME} = -2B_1 w_{\rm f} t_{\rm f}\left(\cos^2\phi\frac{\partial \varepsilon_{xx}}{\partial x} + \sin^2\phi\frac{\partial \varepsilon_{yy}}{\partial x} - \frac{\partial \varepsilon_{zz}}{\partial x}\right)\Delta, \tag{8}$$

where $w_{\rm f}$ is the width of the nanowire. As already noted, $\partial\varepsilon_{xx}/\partial x \approx \partial\varepsilon_{yy}/\partial x$, one finally has the DW velocity

$$v_x = -\frac{1}{\alpha}\frac{\gamma_0 B_1}{\mu_0 M_{\rm s}}\left(\frac{\partial \varepsilon_{xx}}{\partial x} - \frac{\partial \varepsilon_{zz}}{\partial x}\right)\Delta^2 - \frac{\beta}{\alpha}\gamma_0 u J_x. \tag{9}$$

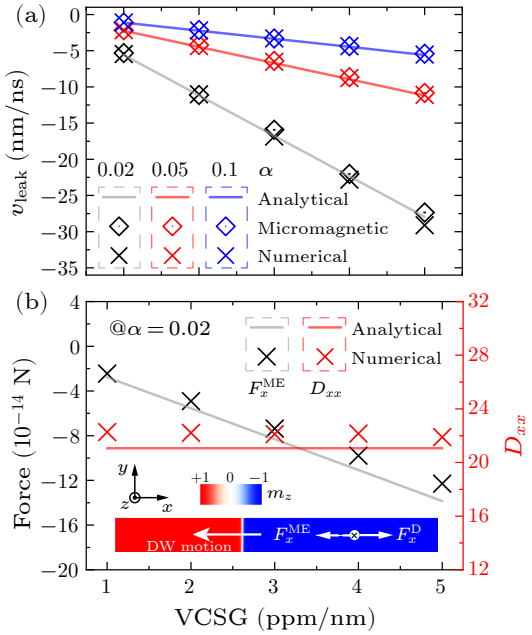

Fig. 2. (a) Velocity $v_{\rm leak}$ as a function of the VCSG strength with different α. (b) $F_x^{\rm ME}$ and D_{xx} as a function of the VCSG strength. Inset: force balance in steady leaky dynamics.

DW Leaky Dynamics under VCSG. In Fig. 2(a), we show the prediction of leaky velocity $v_{\rm leak}$ of the analytical model [solid lines, based on Eq. (9)] together with the results obtained from micromagnetic simulations (square symbols). Furthermore, the corresponding values derived from micromagnetic with a numerical method based on Eq. (5) are also shown in Fig. 2(a) with cross mark symbols (see Section S4 in Supplementary Material for details). As can be observed in Fig. 2(a), all curves rise monotonically with the VCSG strength, but the values are remarkably larger when α is small. This can be understood from Eq. (9), the $v_{\rm leak}$ driven by the VCSG is determined by its strength and $1/\alpha$, increasing VCSG strength and decreasing α will cause an increase in the DW mobility. We would like to note that the results obtained by both the numerical and analytical calculation are in fairly good agreement with the micromagnetic simulations, which indicates that Thiele's formalism we have developed can capture the most relevant features of DW steady motion under VCSG. To further understand the origin of this VCSG-induced DW motion, we investigate how $F_x^{\rm ME}$ and D_{xx} depend

on the VCSG strength. This results, evaluated analytically and numerically, are shown in Fig. 2(b). As can be seen, the F_x^{ME} increases negatively with VCSG strength, thereby increasing the v_{leak}. For the D_{xx}, the analytical one is unchanged with VCSG strength due to the fixed Δ. This reveals that the DW structure will change under different VCSG strengths, a feature not considered in our analytical model, which is the main reason for the discrepancy between the simulation and analytical results shown in Fig. 2(a). The inset of Fig. 2(b) shows a schematic of the force balance on the DW. Notably, in this case, the F_x^{ME} is parallel to the DW motion direction, and F_x^{D} is always anti-parallel to the motion direction. This also simply explains the origin of the DW leaky directions which is consistent with the recent work that the tensile strain favors Néel DW for materials with negative magnetoelastic coupling constant.[23]

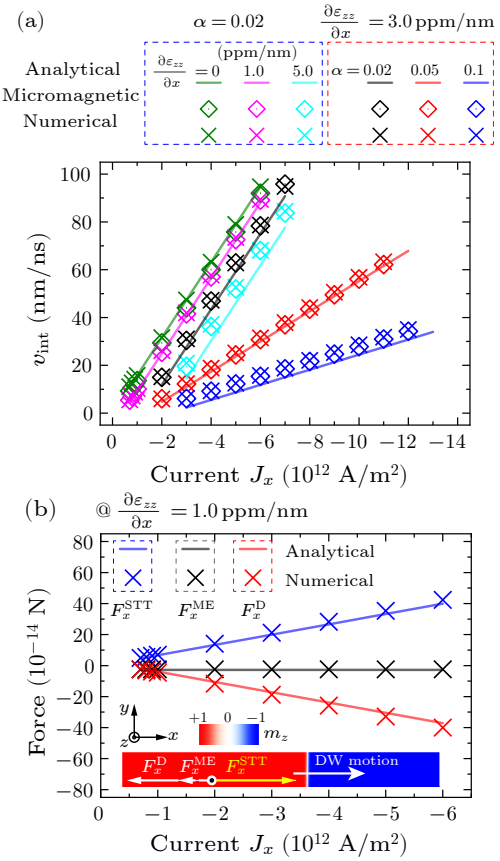

Fig. 3. (a) Velocity v_{int} as a function of J_x with different α and VCSG strengths. (b) F_x^{STT}, F_x^{ME}, and F_x^{D} versus J_x. Inset: force balance in the steady integrating process.

DW Integrated Dynamics with the Combined Effect of STT and VCSG. After proving the DW leaky dynamics solely induced by VCSG, now we focus on the integration process. The integrating velocity v_{int}–J_x curves, for a series of VCSG strength and α combinations, are plotted in Fig. 3(a). One can see that our analytical predictions are still in good agreement with the micromagnetic simulations. We would like to note that, the cutoff of the v_{int}–J_x curves is owing to the DW annihilated at the right end. For both the cases, no Walker breakdown is observed, and the DW mobility remains constant within the ranges of J_x and VCSG strength considered here. Another feature is that a linear increase in v_{int} is obtained in both the cases, but the value of v_{int} is smaller when the VCSG is included. This can be understood by considering the force balance as shown in Fig. 3(b), the F_x^{ME} and F_x^{STT} in the opposite directions, as a result, the VCSG decreases the net force. Definitely, an increase in VCSG strength leads to a much reduction and finally induces a decrease of v_{int}. Therefore, by introducing the VCSG it is possible to modulate the v_{int} efficiently.

DW Stopped Position and Sigmoid Function Generator. Our previous studies have shown that the equilibrium position of DW can be dominated by the VCSG strength,[44] whereas the pinning force induced by VCSG on the DW could affect its initial process of current-driven dynamics. At some point, it would compensate for the F_x^{STT}, and the DW ends up the motion at a given position x_{p}.

In Fig. 4(a), we extract the DW stopped position x_{p} as a function of J_x with different VCSG strengths. As expected, the initial position of the DW increases with VCSG strength. When the J_x increases, the x_{p} gradually moves away from the initial position. Once J_x is larger than a critical value, the current drive DW moves to the right and the position x_{p} rises quickly. This result implies that the mechanism of a DW pinning by a VCSG is different from the one caused by the artificial defects, as the former is dominated by magnetoelastic energy variation. Furthermore, our method is effective and controllable for pinning DW, i.e., a larger VCSG strength needs a strong current to overcome the pinning effect, however, the pinning strength of defects cannot be modulated after fabrication. With the J_x further increasing, the x_{p} trends saturate before being annihilated due to the edge repulsive force. Because of the pining effect and edge repulsion, a nonlinear dependence of x_{p} on the J_x is observed. Fitting the x_{p}-J_x curves by utilizing a shift Sigmoid function $y = (A_1 - A_2)[1 + \exp(\frac{x - x_0}{k})]^{-1} + A_2$ which is essential for solving nontrivial problems in multilayer artificial networks,[53] as the solid line shown in Fig. 4(a). Here, A_1 and A_2 are the fitting parameters corresponding to the initial and saturate DW positions, x_0 and k represent the shift and slope of the x_{p}-J_x curves, respectively. We observe that the DW stopped position successfully follows the Sigmoid function. The x_0 and k at different VCSG strengths are summarized in Fig. 4(b). As can be observed, x_0 can be efficiently controlled by the VCSG, while k is not sensitive to the VCSG strength. The shift in x_0 with an increase in VCSG is a result of higher magnetoelastic force caused by the VCSG, which needed a larger STT force to balance, then yielding a large value of x_0. Meanwhile, the VCSG is almost constant except at two length ends, thus, k is unaffected by VCSG strength. Physically, changing such VCSG to a nonlinear manner can adapt the slope of the Sigmoid function, which is one of the important aspects of neural network training. As shown in Fig. 4(c) and 4(d), various k values were achieved, where the exponential growth of voltage on the electrodes was selected as

indicated by the function $U = \exp[a(x-0.54)]-2$ with parameter a. Mathematically, such the exponential growth voltage can induce nonlinear changed VCSG and the nonlinearity is dependent on the parameter a, see Fig. S2(b) in Section S1 of Supplementary Material. When the parameter a is larger, the applied voltage steps are larger, which induces sharp VCSG changes. Then, because the k depends on how fast the VCSG changes, meanwhile, x_0 shifts to the right, and a change in k can be achieved. Therefore, our proposed devices have shown the potential to implement a tunable Sigmoid activation function generator, which can improve the adaptability of the spintronic neuron.

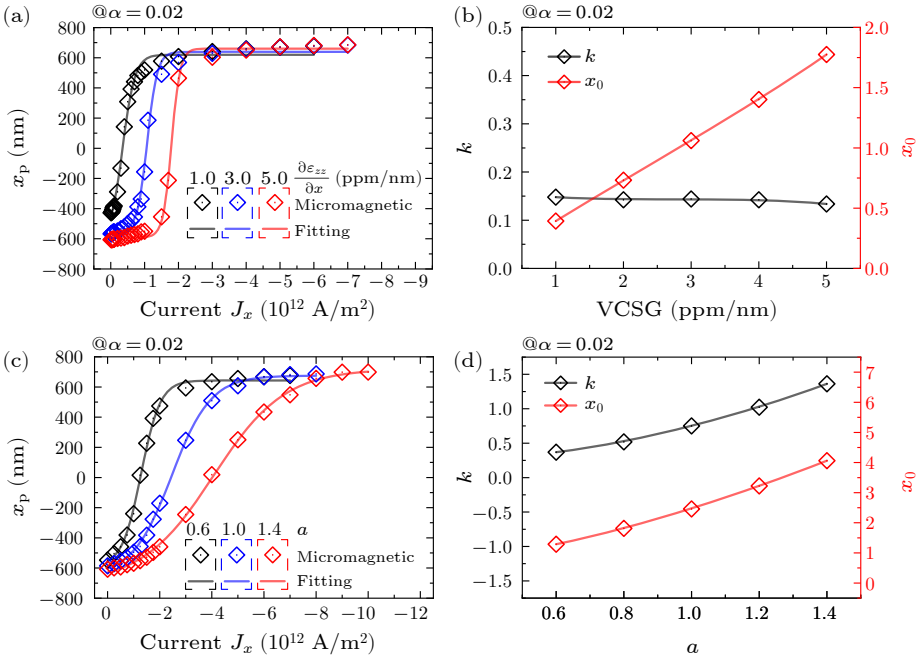

Fig. 4. For the linear changed voltage: (a) $x_{\rm p}$ as a function of J_x with different VCSG strengths, (b) x_0 and k versus VCSG strengths. For the nonlinear one: (c) $x_{\rm p}$–J_x curves with different a, (d) x_0 and k versus a.

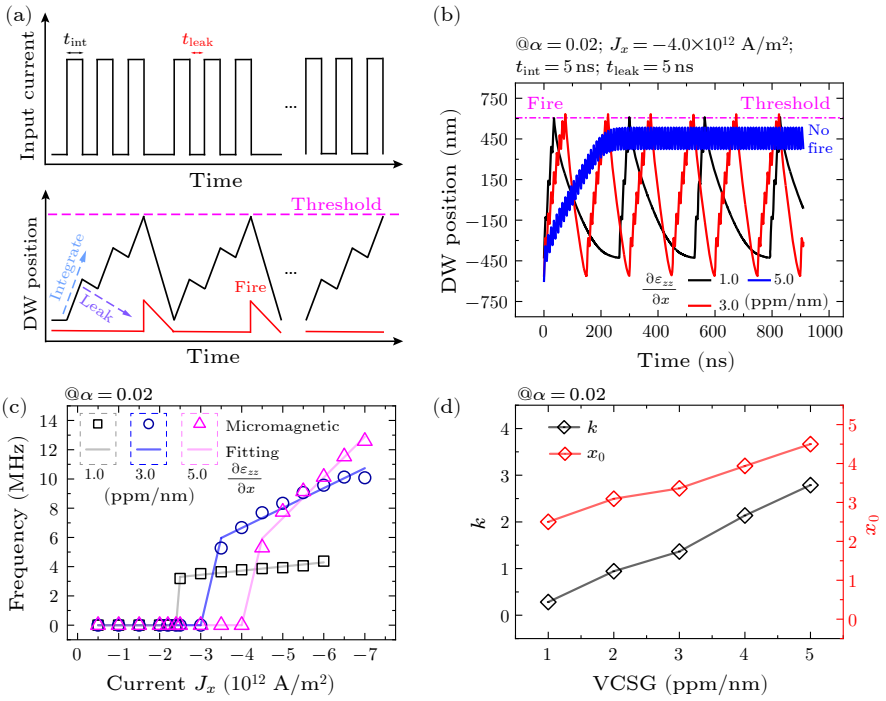

Fig. 5. (a) Concept and operation principle of DW-based LIF neuron. (b) Waveforms of LIF neurons for various VCSG strengths. (c) Spiking frequency versus J_x. (b) The VCSG dependent x_0 and k of the fitting ReLU function.

Tunable LIF Characteristic. The proposed architecture to construct leaky and integrated properties has been fully verified separately, as a final test, we would like to discuss the LIF operation of the DW-based neuron. The input current pulse sequence and the operation principle of the proposed DW-based artificial neuron are presented in Fig. 5(a). Initially, a DW is placed at the pinning position induced by VCSG. Then, a sequence of current pulses is applied. If the current strength is large enough to compensate for the VCSG-induced magnetoelastic force, $F_x^{\rm STT} > F_x^{\rm ME}$, the DW will be moving forward which can be regarded as an integrated process; while $F_x^{\rm STT} < F_x^{\rm ME}$, the DW will be moving back towards the initial position which can be regarded as the leaky process. When the DW moving reaches a threshold, the neuron will fire and output a spike, and then the DW resets to its initial position spontaneously under the VCSG effect. The DW position waveforms for various VCSG strengths are presented in Fig. 5(b). In this simulation, the current pulse density is fixed at $J_x = -4 \times 10^{12}\,\mathrm{A/m^2}$, the time for integral $t_{\rm int} = 5\,\mathrm{ns}$, the time for leaky $t_{\rm leak} = 5\,\mathrm{ns}$, and the fire position $x_{\rm f} = 600\,\mathrm{nm}$. Assume that the DW undergoes a brief reset process that the neuron no longer integrates any input current during reset. As can be observed in Fig. 5(b), when the VCSG strength is 5 ppm/nm, the DW moves in a back-and-forth oscillation around a specific dynamic equilibrium position, which is smaller than the threshold, thus, exhibiting an integrate-leaky process without fire. In other words, the distance of the DW motion corresponding to the integration process as $L_{\rm int} = \int_t^{t+t_{\rm int}} dt v_{\rm int}$ remains relatively equal to the leaky distance $L_{\rm leak} = \int_t^{t+t_{\rm leak}} dt v_{\rm leak}$. Specifically, for the 3 ppm/nm and 1 ppm/nm cases, we find that the LIF behavior is observed. Physically, this can be understood by considering the difference between $v_{\rm int}$ and $v_{\rm leak}$ shown in Figs. 3(a) and 2(a), respectively. For the 5 ppm/nm case, the $v_{\rm int}$ at $J_x = -4 \times 10^{12}\,\mathrm{A/m^2}$ is slightly larger than $v_{\rm leak}$ at VCSG = 5 ppm/nm, thus it is difficult to accumulate the DW position to reach the threshold value, especially when the DW approaching the right edge of the nanostrip where the edge force effected. For the 3 ppm/nm case, the $v_{\rm int}$ at $J_x = -4 \times 10^{12}\,\mathrm{A/m^2}$ is almost twice larger than $v_{\rm leak}$ at VCSG = 3 ppm/nm, thus exhibiting LIF behaviors apparently. The case of 1 ppm/nm is also consistent with the aforementioned one. Therefore, the VCSG can be regarded as a neuron switch, more details of the neuron working phase diagram can be found in Fig. S4 in Section S4 of Supplementary Material.

Then, we investigate the intermodulation between the firing frequency and the VCSG strength, as illustrated in Fig. 5(c). As can be observed, the neuron transforms from the OFF state (zero fire frequency) to the ON state when the applied current exceeds the critical current. Once the neuron fire turns ON, the firing frequency is almost linearly with the increasing spiking current density because the $v_{\rm int}$ linearly increases as the strength of the current increases. In particular, this relationship can be considered as a rectified linear unit (ReLU) type activation function, i.e., $y = 0$ for $x \le x_0$ and $y = k(x - x_0) + b$ for $x > x_0$, which is commonly used in the backpropagation algorithm.[54] Here, b is the fitting parameter corresponding to the minimum fire frequency at state ON, x_0 and k represent the rising point and slope of the frequency–J_x curve. Apparently, the slope of the ReLU function can also be tuned by the VCSG. Therefore, we further study the relationship between the two parameters and the VCSG strength, as summarized in Fig. 5(d). Because the x_0 corresponds to the threshold current, when the integrate-leaky time is fixed (see Fig. S5 in Section S4 of the Supplementary Material for the LIF response under various leaky times), the x_0 increases with increasing VCSG strength. Meanwhile, besides the larger current decrease in the time of DW approaching the threshold position, larger VCSG induces a larger leaky velocity, resulting in a decrease of the self-reset time, thus k increases with the VCSG strength. Therefore, this VCSG tuning capability proves that our proposed schematic can be used to customize the artificial LIF neuron for specific applications.

In conclusion, we have theoretically and numerically investigated the DW dynamics synergist driven by STT and VCSG in a multiferroic heterostructure. The current driven DW dynamics modulated by the VCSG strength verifies the feasibility of implementing the LIF behavior of the proposed artificial neurons. Specifically, the DW automatically returns to its initial position without current, which can be analogous to the self-resetting function. Micromagnetic simulation and analytical model show that the leaky velocity increases with the VCSG strength and that the integral velocity depends on the combined effect of VCSG and STT. Moreover, we find that the current-dependent spiking frequency follows the ReLU-type activation function, and successfully performs the tunable properties of the ReLU function by VCSG, which provides a route to design the reconfigured artificial neurons and further reduces the complexity of the device. Furthermore, the scheme could also be implemented for design of a tunable Sigmoid activation function generator with nonlinear VCSG. From a broader perspective, we believe that the potential application of our proposed schema goes beyond artificial neural devices, but it exhibits an additional approach to control the DW dynamics, which could have a strong impact on the implementation of DW-based nonvolatile memory and logic devices.

Acknowledgments. This work was supported by the National Natural Science Foundation of China (Grant Nos. 51902300, 11972333, and 11902316), the Zhejiang Provincial Natural Science Foundation of China (Grant Nos. LY21F010011, LZ19A020001, and LZ23A020002), and the Fundamental Research Funds for the Provincial Universities of Zhejiang (Grant Nos. 2021YW02 and 2022YW88). Guo-Liang Yu also acknowledges the Start-up Foundation and Young Science & Technology Talent Program from China Jiliang University. The Key Laboratory of Electromagnetic Wave Information Technology and Metrology of Zhejiang Province supported the simulations.

References

[1] Parkin S S P, Hayashi M, and Thomas L 2008 *Science* **320** 190

[2] Bahri M A, Hinaai M A, and Harthy T A 2023 *Chin. Phys. B* **32** 127508
[3] Allwood D A, Xiong G, Faulkner C C, Atkinson D, Petit D, and Cowburn R P 2005 *Science* **309** 1688
[4] Luo Z C, Hrabec A, Dao T P, Sala G, Finizio S, Feng J X, Mayr S, Raabe J, Gambardella P, and Heyderman L J 2020 *Nature* **579** 214
[5] Lin H, Xu N, Wang D, Liu L, Zhao X, Zhou Y, Luo X, Song C, Yu G, and Xing G 2022 *Adv. Intell. Syst.* **4** 2200028
[6] Sato N, Schultheiss K, Körber L, Puwenberg N, Mühl T, Awad A A, Arekapudi S S P K, Hellwig O, Fassbender J, and Schultheiss H 2019 *Phys. Rev. Lett.* **123** 057204
[7] Cheng M, Yuan X, Li S, Chen C, Zhang Z, Yu Z, Liu Y, Lu Z, and Xiong R 2020 *Nanotechnology* **31** 235201
[8] Wang D, Wang Z, Jiang S, Liu L, Lin H, Zhang Y, Tang R, Luo X, and Xing G 2023 *Mater. Today Electron.* **6** 100065
[9] Sharad M, Augustine C, Panagopoulos G, and Roy K 2012 *IEEE Trans. Nanotechnol.* **11** 843
[10] Kaushik D, Singh U, Sahu U, Sreedevi I, and Bhowmik D 2020 *AIP Adv.* **10** 025111
[11] Hong J, Li X, Xu N, Chen H, Cabrini S, Khizroev S, Bokor J, and You L 2020 *Adv. Intell. Syst.* **2** 2000143
[12] Wang C, Wang Z, Wang M, Zhang X, Zhang Y, and Zhao W 2020 *IEEE Trans. Electron Devices* **67** 2621
[13] Liu S, Bennett C, Friedman J, Marinella M, Paydarfar D, and Incorvia J A 2021 *IEEE Magn. Lett.* **12** 1
[14] Mah W L W, Kumar D, Jin T, and Piramanayagam S N 2021 *J. Magn. Magn. Mater.* **537** 168131
[15] Vernier N, Allwood D A, Atkinson D, Cooke M D, and Cowburn R P 2004 *Europhys. Lett.* **65** 526
[16] Thiaville A, Nakatani Y, Miltat J, and Vernier N 2004 *J. Appl. Phys.* **95** 7049
[17] Wang X R, Yan P, Lu J, and He C 2009 *Ann. Phys.* **324** 1815
[18] Chen C, Piao H G, Shim J H, Pan L Q, and Kim D H 2015 *Chin. Phys. Lett.* **32** 087502
[19] Liu T T, Hu Y F, Liu Y, Jin Z J Y, Tang Z H, and Qin M H 2022 *Rare Met.* **41** 3815
[20] Sohn H, Nowakowski M E, Liang C Y, Hockel J L, Wetzlar K, Keller S, McLellan B M, Marcus M A, Doran A, Young A, Kläui M, Carman G P, Bokor J, and Candler R N 2015 *Acs Nano* **9** 4814
[21] Wang X S, Yan P, Shen Y H, Bauer G E W, and Wang X R 2012 *Phys. Rev. Lett.* **109** 167209
[22] Dean J, Bryan M T, Cooper J D, Virbule A, Cunningham J E, and Hayward T J 2015 *Appl. Phys. Lett.* **107** 142405
[23] Fattouhi M, Garcia-Sanchez F, Yanes R, Raposo V, Martinez E, and Lopez-Diaz L 2022 *Phys. Rev. Appl.* **18** 044023
[24] Kim D H, Moon K W, Yoo S C, Min B C, Shin K H, and Choe S B 2013 *IEEE Trans. Magn.* **49** 3207
[25] Liu S, Xiao T P, Cui C, Incorvia J A C, Bennett C H, and Marinella M J 2021 *Appl. Phys. Lett.* **118** 202405
[26] Lone A H, Li H R, El-Atab N, Setti G, and Fariborzi H 2023 *IEEE Trans. Electron Devices* **70** 6293
[27] Wang D, Tang R F, Lin H, Liu L, Xu N, Sun Y, Zhao X F, Wang Z W, Wang D D, Mai Z H, Zhou Y J, Gao N, Song C, Zhu L J, Wu T, Liu M, and Xing G Z 2023 *Nat. Commun.* **14** 1068
[28] Zhang Z, Sun J, Zheng Z, Lin K, Zhang K, Wang J, Zhang Y, Zhao W, and Zhang Y 2022 *IEEE Electron Device Lett.* **43** 1567
[29] Zhang Z, Lin K, Zhang Y, Bournel A, Xia K, Kläui M, and Zhao W 2023 *Sci. Adv.* **9** eade7439
[30] Kumar D, Chung H J, Chan J P, Jin T L, Lim S T, Parkin S S P, Sbiaa R, and Piramanayagam S N 2023 *ACS Nano* **17** 6261
[31] Wang D, Wang Z, Xu N, Liu L, Lin H, Zhao X, Jiang S, Lin W, Gao N, Liu M, and Xing G 2022 *Adv. Sci.* **9** 2203006
[32] Bhowmik D, Saxena U, Dankar A, Verma A, Kaushik D, Chatterjee S, and Singh U 2019 *J. Magn. Magn. Mater.* **489** 165434
[33] Sengupta A, Shim Y, and Roy K 2016 *IEEE Trans. Biomed. Circuits Syst.* **10** 1152
[34] Yu Z Y, Shen M K, Zeng Z M, Liang S H, Liu Y, Chen M, Zhang Z H, Lu Z H, You L, Yang X F, Zhang Y, and Xiong R 2020 *Nanoscale Adv.* **2** 1309
[35] Agrawal A and Roy K 2019 *IEEE Trans. Magn.* **55** 1400107
[36] Brigner W H, Hu X, Hassan N, Bennett C H, Incorvia J A C, Garcia-Sanchez F, and Friedman J S 2019 *IEEE J. Explor. Solid-State Comput.* **5** 19
[37] Brigner W H, Hassan N, Jiang W L, Hu X, Saha D, Bennett C H, Marinella M J, Incorvia J A C, Garcia-Sanchez, and Friedman J S 2019 *IEEE Trans. Electron Devices* **66** 4970
[38] Hassan N, Hu X, Jiang W L, Brigner W H, Akinola O G, Garcia-Sanchez F, Pasquale M, Bennett C H, Incorvia J A C, and Friedman J S 2018 *J. Appl. Phys.* **124** 152127
[39] Wang Y, Xu H, Wang W, Zhang X, Wu Z, Gu R, Li Q, and Liu Q 2022 *IEEE Electron Device Lett.* **43** 631
[40] Guo T, Pan K, Sun B, Wei L, Yan Y, Zhou Y N, and Wu Y A 2021 *Mater. Today Adv.* **12** 100192
[41] Shaban A, Bezugam S S, and Suri M 2021 *Nat. Commun.* **12** 4234
[42] Bryan M T, Dean J, and Allwood D A 2012 *Phys. Rev. B* **85** 144411
[43] Yu G, Shi S, Peng R, Guo R, Qiu Y, Wu G, Li Y, Zhu M, and Zhou H 2022 *J. Magn. Magn. Mater.* **552** 169229
[44] Yu G, He X, Qiu Y, Wu G, Guo R, Zhu M, and Zhou H 2022 *AIP Adv.* **12** 035036
[45] de Araujo C I L, Alves S G, Buda-Prejbeanu L D, and Dieny B 2016 *Phys. Rev. Appl.* **6** 024015
[46] Qiao Y, Zhang Y, and Yuan Z 2023 *New J. Phys.* **25** 033031
[47] Hu J M, Yang T, and Chen L Q 2018 *Npj Comput. Mater.* **4** 62
[48] Duflou R, Ciubotaru F, Vaysset A, Heyns M, Sorée B, Radu I P, and Adelmann C 2017 *Appl. Phys. Lett.* **111** 192411
[49] Di K, Zhang V L, Lim H S, Ng S C, Kuok M H, Qiu X, and Yang H 2015 *Appl. Phys. Lett.* **106** 052403
[50] Igarashi J, Llandro J, Sato H, Matsukura F, and Ohno H 2017 *Appl. Phys. Lett.* **111** 132407
[51] Li R, Zhang S, Luo S, Guo Z, Xu Y, Ouyang J, Song M, Zou Q, Xi L, Yang X, Hong J, and You L 2021 *Nat. Electron.* **4** 179
[52] Yu G Q, Wang Z X, Abolfath-Beygi M, He C L, Li X, Wong K L, Nordeen P, Wu H, Carman G P, Han X F, Alhomoudi I A, Amiri P K, and Wang K L 2015 *Appl. Phys. Lett.* **106** 072402
[53] Yang S, Shin J, Kim T, Moon K W, Kim J, Jang G, Hyeon D S, Yang J, Hwang C, Jeong Y, and Hong J P 2021 *NPG Asia Mater.* **13** 11
[54] Chen Y B, Yang X K, Yan T, Wei B, Cui H Q, Li C, Liu J H, Song M X, and Cai L 2020 *Chin. Phys. Lett.* **37** 078501